Active model-based suppression of secondary ride for electric vehicles with in-wheel motors

Shota Yamada[1], *Member, IEEE,* Thomas Beauduin[1], *Member, IEEE,* Hiroshi Fujimoto[1], *Senior member, IEEE,* Takeshi Kanou[2], and Etsuo Katsuyama[2]

Abstract—In vehicle motion control, the objective is to improve both dynamic performance and ride comfort through vibration analysis and compensation. Conventional drivetrains (combustion engines or on-board eletric motors) can only suppress primary modes (0.1-3 Hz) due to their limited torque response though the transmission shaft. In the case of electric vehicles with in-wheel motors (IWM), the *shaft-less* drivetrain enables besides primary also the active suppression of secondary ride modes (3-25 Hz). These compact and light-weight drivetrains have a higher unsprung mass and therefore require advanced suppression control methods that encompass both vibration regimes (0.1-25 Hz). The approach presented in this paper aims to suppress secondary ride in IWM vehicles through experimental model analysis and model-based control. In this study, the frequency characteristics of a Toyota IWM vehicle are experimentally analyzed on vibration test rigs and subsequently in multiple driving conditions. Based on the identified frequency responses, a model-based longitudinal acceleration control method is then analytically derived to suppress the vibration over a wide frequency band. The proposed technique is validated through experiments on Toyota's IWM prototype vehicles.

Index Terms—Electric vehicles, In-Wheel Motor, vehicle dynamics, modal analysis, vibration suppression control.

I. INTRODUCTION

VEHICLE motion control aims to improve both dynamic performance and ride comfort through experimental modal analysis and vibration compensation. The vibration spectrum of vehicles is classified into two main regions: 1) primary modes (0.1-3 Hz) including the heave, pitch, and roll and 2) secondary modes (3-25 Hz) reported as unpleasant to passengers [1], [2]. Conventional motion control studies rely on active suspension systems to add controllable degrees-of-freedom and suppress predominantly the primary ride [3]. The main drawbacks impeding the widespread adoption of these methods is the additional cost, hardware reliability issues and severe constraints imposed on the suspension design.

Recently, the flexibility of electric drives enables power-trains with distributed traction capable of independent control of the driving force at each wheel and, through the suspension reaction force, the sprung mass motion. Currently, distributed traction from On-Board Motors (OBM), which adopt a drive-train configuration similar to conventional Internal Combustion Engine (ICE) vehicles, are reaching the market [4]. The distributed drives add controllable degrees-of-freedom at no additional cost and can be effectively utilized to suppress primary vibration modes to improve vehicle handling and comfort [5].

Nevertheless, conventional drivetrains with distributed traction from OBMs can only suppress primary modes due to their limited torque response through the transmission shaft. The torsional resonance of the driveshaft and joints required to transmit the power from the body to the unsprung commonly lays around 4 Hz for passenger cars [6]. In the case of electric vehicles with in-wheel motors (IWM), the distributed *shaft-less* drivetrain enables besides primary also the active suppression of secondary ride modes. Moreover, moving the drive from the body to the hub increases the degree of freedom in the interior layout of the vehicle and reduces the total weight of the drivetrain [7]. Several recent studies demonstrate the potential of compact IWM systems to suppress primary modes (mostly heave, pitch and yaw) for superior vehicle performance [8], [9].

Albeit, this comes at the expense of a higher unsprung mass increasing the vibration modes and thus, imposing the implementation of active suppression methods for the overall vibration regime (0.1-25 Hz). Some studies propose additional structures with springs and annular bushings in the wheel to improve ride comfort [10], [11]. The few higher frequency control methods found in literature to compensate secondary ride in IWMs can be categorized in a) vertical and b) longitudinal vibration control methods. Katsuyama *et al.* proposed a robust industrial feedback control method based on the unsprung vertical velocity to obtain a virtual negative sky-hook damper control [12]. Ohno *et al.* instead proposed a backlash compensation method to attenuate the impact on the gear and indirectly limit the excitation of the longitudinal vibration [13]. Alternatively, Takesaki *et al.* describes a pitch rate feedback control with a specified step settling feedforward (FF) control for longitudinal vibration [14]. They assume the longitudinal vibration is caused by the bushings, albeit the method is only evaluated by stepwise braking simulations in time domain without clear modal suppression. Finally, Fukudome presents a suitable longitudinal vibration suppression method based on relative velocity feedback with experimental validation [15]. The method suppresses the main longitudinal mode directly and consistently at the expense of amplifying higher order modes requiring a trade-off to balance the impact. Regardless of its shortcoming, the method outperforms the previous studies and is further described, compared and evaluated with the proposed method in this paper.

[1]The University of Tokyo, 5-1-5 Kashiwanoha, Kashiwa, Chiba, 277-8561, Japan. yamada.s@edu.k.u-tokyo.ac.jp, thomas.beauduin15@ae.k.u-tokyo.ac.jp, fujimoto@k.u-tokyo.ac.jp

[2]Toyota Motor Corporation, 1200 Mishuku, Susono, Shizuoka, 410-1193, Japan. takeshi_kanou_aa@mail.toyota.co.jp, etsuo_katsuyama@mail.toyota.co.jp

Despite the recent surge in IWM research, most studies are limited to conventional motion control approaches due to the lack of electric drivetrain modal analysis [16]. The different IWM control studies compared above are based principally on time domain identification methods and do not perform any modal comparison or analysis. Tuononen *et al.* compare the frequency characteristics of electric vehicles with different drivetrain configuration including OBMs and IWMs, but only through simulations [17]. One of the few experimental studies conducted by Montonen *et al.* identifies the resonance in a series electric hybrid bus, but is limited in scope to the torsional mode [18]. Hence, experimental analysis or even higher-order simulations of electric drivetrain dynamics in multiple degrees-of-freedom are scarce and incomplete, yet essential for advanced motion control.

This paper aims to a) experimentally identify higher-order IWM vehicle dynamics and b) propose a model-based longitudinal acceleration control method for secondary ride suppression. First, the experimental frequency characteristics of IWM vehicle are valuable not only for analysis, but also to exploit the higher motion performance potential of IWM drivetrains. Second, the control of longitudinal dynamics is little studied as it is out-of-reach for conventional ICE and OBM vehicles, yet essential for IWM vehicles handling and ride comfort.

In this objective, the two main paper contributions are a) an extensive experimental modal analysis based on accurate frequency identification methods and b) a novel model-based two degrees-of-freedom acceleration control strategy. This paper is an advanced study of the initial results published in [19] and [20] with more literature review, additional experiments, and analyses.

In the first contribution, described in sections II and III, a developed IWM unit is experimentally analyzed on several setups in multiple degrees-of-freedom. The IWM quarter-car unit is first tested on a motor bench to torque input, then an IWM vehicle is evaluated on a vibration test rig to road-disturbances and finally the vehicle is evaluated on a test track in driving conditions. In each state, the coupled dynamics in rotational, longitudinal motion directions are accurately measured over a wide-frequency range and the main resonances analyzed for control design.

In the second contribution, described in sections IV and V, a novel high-bandwidth longitudinal acceleration control method is outlined and subsequently assessed through experiments. The method is based on the models identified in the previous sections, which show an 11 Hz longitudinal mode deteriorating ride comfort and a 26 Hz coupled rotational mode degrading the motion control performance. The proposal combines a FF controller for torque input, a state feedback controller and notch filter for road-disturbances and modeling errors and a dead-time compensated state observer for Controller Area Network (CAN) communication delay. The proposed method is compared with the conventional method in literature [15] and the advantages are validated through experiments on the IWM vehicle.

II. SYSTEM MODELING

This section describes a quarter-car drivetrain model for the vehicle dynamics of EVs with independent drives. The model combines the drivetrain rotational dynamics and a suspension model in longitudinal directions. The model schematics are shown in Fig. 1a and the definitions of the parameters listed in Table 1b. Please note that the viscosity elements such as the suspension damper are excluded from the figure to improve visibility.

The rotational motion equations are described as follows

$$J_m\ddot{\theta}_m + C_\theta(\dot{\theta}_m - \dot{\theta}_h) + K_\theta(\theta_m - \theta_h) = T_m,$$
$$J_h\ddot{\theta}_h - C_\theta(\dot{\theta}_m - \dot{\theta}_h) - K_\theta(\theta_m - \theta_h) = -rF_{d,x}. \quad (1)$$

In which, the fixed transmission gear ratio of 8 was incorporated in θ_h as a gear-reduced angle for the sake of simplicity. Additionally, the higher-order tire rotational modes (e.g. $K_{t\theta}$), although identified in experiments, are omitted here in the equations for the sake of simplicity considering their high natural frequency (>25 Hz).

At the tire-road interface, a driving force $F_{d,x}$ is applied though the tire causing a reaction force. Hence, the longitudinal motion equations are defined as

$$M_u\ddot{x}_u + C_{s,x}(\dot{x}_u - \dot{x}_b) + K_{s,x}(x_u - x_b) = F_{d,x},$$
$$M_b\ddot{x}_b - C_{s,x}(\dot{x}_u - \dot{x}_b) - K_{s,x}(x_u - x_b) = 0. \quad (2)$$

The rotational and longitudinal motions are coupled by the traction force $F_{d,x}$ when the tire is in contact with the ground. Considering the slip-ratio λ at the time of driving, the following equations are derived

$$\lambda = \frac{r\dot{\theta}_h - \dot{x}_u}{r\dot{\theta}_h}, \quad (3)$$

$$\dot{x}_u = (1-\lambda)r\dot{\theta}_h, \quad (4)$$

$$\int_0^{\Delta t} \frac{dx_u}{dt}dt = r\int_0^{\Delta t}(1-\lambda)\frac{d\theta_h}{dt}dt. \quad (5)$$

Assuming that the slip-ratio fluctuation over a finite time Δt is negligible, the following formulas are derived

$$\int_0^{\Delta t} \frac{dx_u}{dt}dt = r(1-\lambda)\int_0^{\Delta t}\frac{d\theta_h}{dt}dt, \quad (6)$$

$$x_u = r(1-\lambda)\theta_h \stackrel{\text{def}}{=} R\theta_h. \quad (7)$$

where the variable conversion factor from rotational to longitudinal motion is defined as R. Assuming that fluctuations in slip-ratio between Δt is negligible, one obtains

$$\dot{x}_u = (R\dot{\theta}_h) = \dot{R}\theta_h + R\dot{\theta}_h \simeq R\dot{\theta}_h. \quad (8)$$

The resulting transfer functions from the motor angle to the motor torque and from the longitudinal unsprung acceleration to the motor torque is

$$\frac{\theta_m}{T_m} = \frac{1}{J_m s^2}\frac{s^4 + a_1 s^2 + a_0}{s^4 + b_1 s^2 + b_0}, \quad (9)$$

$$\frac{\ddot{x}_u}{T_m} = \frac{RK_\theta}{J_m}\frac{s^2 + \frac{K_{s,x}}{M_b}}{s^4 + b_1 s^2 + b_0}. \quad (10)$$
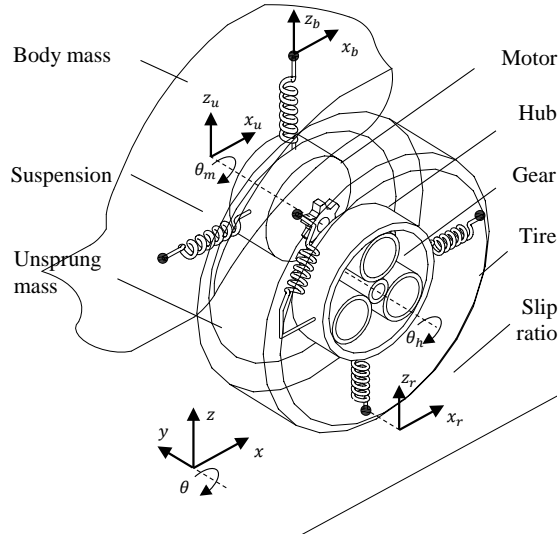
(a) IWM quarter-car model and coordinate system.

Symbol	Description	Value	Unit
M_u	unsprung mass	80	kg
M_b	quarter-car body mass	400	kg
J_m	motor inertia	1.2	kg.m^2
J_h	hub interia (incl. tire)	0.8	kg.m^2
K_t, C_t	tire stiffness/damping	-	N/m(/s)
K_s, C_s	suspension stiffness/..	-	N/m(/s)
K_θ, C_θ	shaft stiffness/damping	-	Nm/rad(/s)
r	tire radius	0.3	m
x_u	unsprung mass motion	-	m
x_b	body mass motion	-	m
x_r	road/tire motion	-	m
θ_m, θ_h	motor/wheel hub angle	-	rad
T_m	motor torque	± 180	Nm
$F_{d,x}$	driving force on road	-	N
λ	tire slip ratio	-	-

(b) List of plant parameters and degrees-of-freedom.

Fig. 1: System modeling including rotational, longitudinal dynamics. The main specification of the IWM vehicle used for experiments in this study are shown in the plant parameter values.

$$a_1 = \frac{K_\theta + rRK_{s,x}}{J_h + rRM_u}, \quad a_0 = \frac{K_{s,x}K_\theta}{(J_h + rRM_u)J_mM_b},$$

$$b_1 = \frac{K_\theta}{M_b} + \frac{K_\theta + rRK_{s,x}}{J_h + rRM_u} + \frac{K_\theta}{J_m},$$

$$b_0 = \frac{(J_m + J_h) + rR(M_u + M_b)}{(J_h + rRM_u)J_mM_b}K_{s,x}K_\theta,$$

where $C_{s,x} = 0$ and $C_\theta = 0$, to improve visibility. The transfer functions express the coupled dynamics between the rotational and longitudinal motion.

For sufficiently large $K_{s,x}$ and K_θ, one obtains the following conventional expression shown in [21] by substituting $R = r(1 - \lambda)$, thus validating the approach,

$$\frac{\ddot{\theta}_m}{T_m} = \frac{1}{(J_m + J_h) + r^2(M_u + M_b)(1 - \lambda)}. \tag{11}$$

These equations demonstrate that the quarter-car dynamics are coupled at the tire-road interface and thus, a function of the slip-ratio. Although, in the context of this study, the slip ratio fluctuations are assumed limited and modeled as temporal resonance uncertainties to be accounted for in the control design. This assumption is reasonable considering that any outer-loop traction control will distribute the driving force to low-slippage only quarter-car dynamics.

Based on the experimental IWM vehicle parameters shown in Table 1b and typical OBM vehicle parameters, the frequency characteristics for both a OBM and an IWM drivetrain are simulated in Fig. 2 based on (9). The rotational half-shaft mode (4 Hz) limiting the torque response of OBM drivetrains is clearly seen in the low frequency range. In the case of IWM drivetrain, this limitation is alleviated (25 Hz), although the increase in unsprung mass brings the longitudinal mode into the mid-frequency range (10 Hz) causing discomfort for the vehicle occupants.
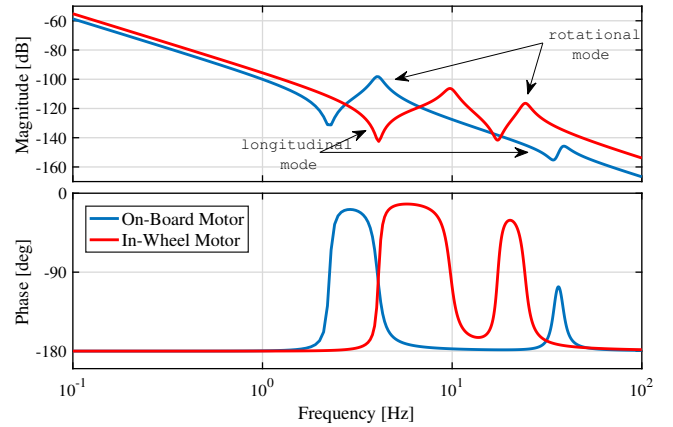

Fig. 2: Frequency response from motor angle to motor torque for both OBM and IWM drivetrains.

III. EXPERIMENTAL MODAL ANALYSIS

The vehicle dynamics of IWM drivetrains are analyzed in this section for a Toyota experimental vehicle on A) a quarter-car motor bench, B) a four-poster test rig, and C) a cobbled test tracks. The dynamics are analyzed in longitudinal directions and through both motor excitations (force) and road disturbances (position).

### A. Quarter-car on test bench

The single wheel and motor setup shown in Fig. 3a has a double wishbone type suspension and an IWM unit described in Fig. 3b identical to the experimental vehicle in Fig. 5a. In the experiments, the electric motor is excited with a custom multisine, motor velocity $\dot{\theta}_m$ is measured by the motor resolver and the motor torque T_m is obtained from the measured current.
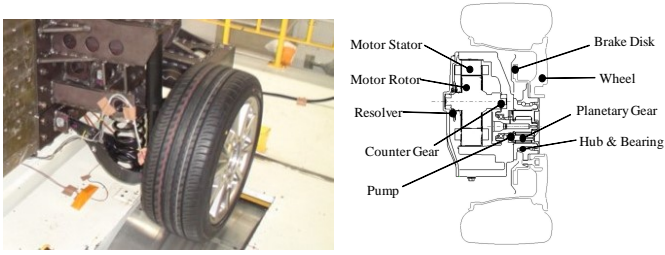
(a) Quarter-car motor bench. (b) IWM unit schematic.

Conditions	Description
input motor output sensor excitation	I-PMSM: 55 kW, gear ratio 8 resolver: 12 bit, 400 Hz multi-sine: 1.6-80 Hz
fitting method model type	Non-linear Least Squares (NLS) 4/5 plant order, 4/4 delay approx.

(c) Experimental conditions and modelling parameters.
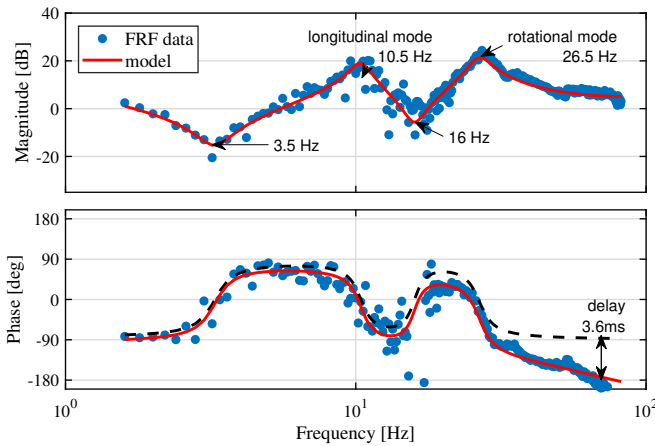
(d) Rotational dynamics ($\dot{\theta}_m/T_m$).

Fig. 3: The quarter-car motor bench experiments to obtain the IWM's frequency response model of the rotational dynamics to motor excitation.

(a) Four-poster test rig. (b) Magnified view.

Conditions	Description
input motor output sensor excitation signal	hydraulic posts: 20 kN, ±100 mm accelerometers: 14 bit, 244 Hz multi-sine: 0.5-30 Hz
fitting method model type	Boot-strapped Least Square (BTLS) 4/4 plant, no delay approx.

(c) Experimental conditions and modelling parameters.
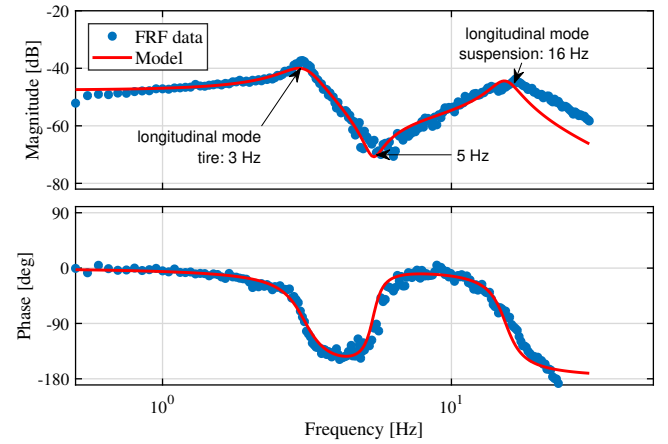
(d) Longitudinal dynamics (x_u/x_r).

Fig. 4: The test rig experiments for the IWM's frequency response model of the longitudinal dynamics to road-disturbances.

The frequency response function (FRF) from the motor torque to the motor velocity is measured and fitted for (9) in Fig. 3d. The rotational mode resulting from the gear flexibility in the IWM drivetrain is identified and fitted at 26.5 Hz. The high unsprung mass brings the longitudinal mode into the mid-frequency range (10.5 Hz) causing discomfort for the passenger. The road-tire contact interface couples the motions incorporating the longitudinal mode into the dynamics seen from the motor side. Consequently, the longitudinal mode becomes the dominant resonance to consider in vibration control design for IWMs instead of the rotational one typical in OBMs (see Fig. 2).

B. Vehicle on test rig

The test rig shown in Fig. 4a consists of four actuators, one for each wheel, able to reproduce, for a car at standstill, a running condition on a certain road profile [22]. The purpose is to accurately measure the IWM's dynamic response to road-disturbance only with custom designed periodic multisine excitations to achieve high data reliability. The test rig excites the vehicle through independent longitudinal road-input positions and measures the acceleration of unsprung mass at each quarter-car with external mounted accelerometers.

The FRF from road position to unsprung position is shown in Fig. 4d. The first resonance, identified at 3 Hz, arises from the longitudinal tire dynamics, which suspend the sprung and unsprung mass on the actuated base. The second resonance is the longitudinal suspension mode measured at 10.5 Hz in Fig. 3d, albeit shifted up to 16 Hz due to the input change from motor torque to road position. With a road-side position input, i.e. disturbances, the tire ring mass is assumed infinite and fixed to the road displacements, which results in a resonance frequency shift up.
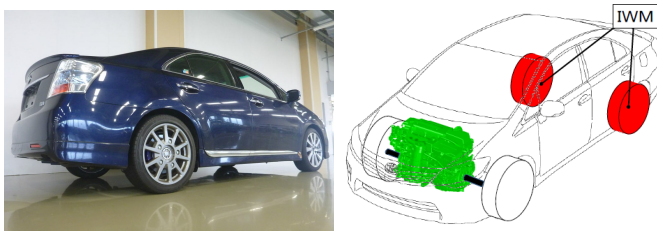
(a) Experimental Toyota SAI.

(b) Drivetrain configuration.
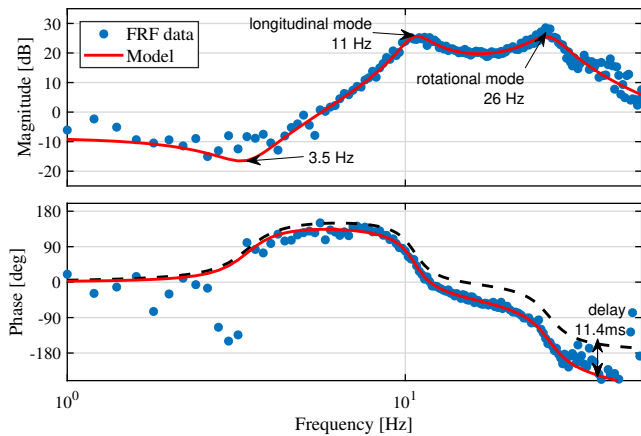
Conditions	Description
input motor output sensor excitation signal	IWM only: 2x55 kW, gear ratio 8 accelerometers: 14 bit, 244 Hz multi-sine: 1-50 Hz or cobbles at 50 km/h
fitting method model type	Boot-strapped Least Square (BTLS) 4/4 plant, 4/4 delay approx.

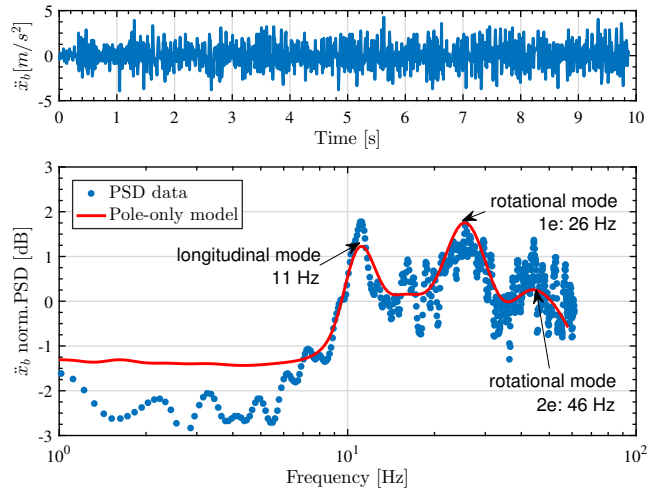(c) Experimental conditions and modelling parameters.

(d) $\ddot{x}_u/T_m$

(e) PSD of $\ddot{x}_b$

Fig. 5: Overview of the test track experiments for the IWM's frequency response model of the longitudinal dynamics to motor excitation in both shaking and driving conditions.

C. Vehicle on test track

The Toyota test vehicle shown in Fig. 5a is rear driven by an IWM powertrain. It serves as a test vehicle to conduct experiments in two states: a) motor torque only input conditions, i.e. shaking at stand-still, and b) road disturbances input conditions, i.e. driven at constant velocity.

1) Shaking conditions: The test vehicle is laden with four passengers and excited through the motor torque with stationary multisines on an even road surface, i.e. no road disturbances. The measured FRF and identified model from unsprung longitudinal acceleration to motor torque are shown in Fig. 5d and described by (10). The response is in accordance with the previous results obtained on both the test bench, the resonance modes arise from coupled longitudinal and rotational dynamics. Moreover, a significant dead time is measured, caused by the CAN communication in the vehicle control architecture, and modeled through the phase margin reduction at higher frequencies. Note, the phase delay identified in the frequency domain (see black dotted line) is the average CAN delay and is used in the observer designed in the following section.

2) Driving conditions: The laden vehicle is driven at constant velocity (50 km/h) over a cobbled road test track with a road profile type D accoding to ISO 8608 [23]. In these experiments the input is not measured, hence, the longitudinal sprung acceleration is assessed in Fig. 5e. The upper figure of Fig. 5e shows the time domain signal of the longitudinal

sprung acceleration. The lower figure shows Power Spectral Density (PSD) of the responses. The road profile is a decreasing function of the spatial frequency and does not contain any peaks that could lead to additional, structurally unrelated modes [24]. The longitudinal resonances arise at both 11 and 16 Hz, as seen on the test bench and the test rig, due to the combined motor torque and road disturbance input to the driving vehicle. Concurrently, the higher frequency rotational dynamics appear at 26 and 46 Hz, as seen on the test bench, due to the IWM torque input and road-contact coupling.

IV. LONGITUDINAL VIBRATION SUPPRESSION CONTROL

The different vibration control designs for IWM drivetrains are described in this section comparing A. the conventional relative velocity feedback method from literature with B. a proposed model-based high-bandwidth controller.

A. Conventional method

The modal analysis in the previous section demonstrated that the main vibration in IWM drivetrains is the longitudinal resonance situated around 11 Hz. The state-of-the-art relative velocity feedback method, proposed by Fukudome in [15], effectively adds a tunable damper to compensate that first mode. Considering the mode is caused by the compliance of the bushings connecting the suspension arm and the vehicle body, relative velocity between sprung and unsprung mass is

(a) Conventional method.
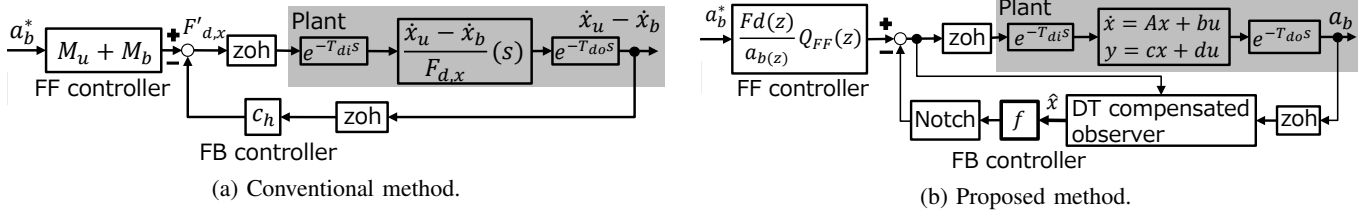
(b) Proposed method.

Fig. 6: Block diagrams of the longitudinal vibration suppression control methods.

fed back to suppress the vibration. The control input for this method is expressed as follows

$$F'_{d,x} = -c_h(\dot{x}_u - \dot{x}_b), \tag{12}$$

where c_h is a tunable relative velocity feedback gain shown in the block-diagram in Fig. 6a with the plant model (2). Note, the conventional feedback (FB) controller is augmented in this study with a feeforward (FF) controller for DC gain compensation. Also, the input and output delay are taken into consideration indicated as T_{di} and T_{do}, respectively. The closed-loop transfer function is then expressed as

$$\frac{a_b}{F'_{d,x}} = \frac{C_{s,x}s + K_{s,x}}{M_u M_b s^2 + ((M_u + M_b)C_{s,x} + M_b c_h)s + (M_b + M_u)K_{s,x}}. \tag{13}$$

The conventional method introduces a single gain c_h, which enables experimental tuning without knowing the plant parameter values. However, due to its simplicity, the method does not account for and excites the higher-frequency rotational mode shown in Fig. 5d. This requires the designer to trade-off phase margin for higher longitundinal damping gain, c_h. As a result, the method's vibration suppresion performance is bounded and its vehicle motion performance limited.

B. Proposed method

The precise modeling and experimental modal analysis in previous sections enable the design of higher-bandwidth model-based controllers. In this study, a control method is proposed that consists of three components: a 4th-order FF controller, a 2nd-order state FB controller with notch filter for the rotational mode and a dead-time compensated observer (see Fig. 6b).

1) FF controller: To improve vehicle motion performance, a 4th-order FF controller is designed based on the inverse model of the plant encompassing the 11 Hz longitudinal and 26 Hz rotational mode. A low-pass filter Q_{FF} is then introduced for realization effectively increasing the control order to six.

2) State FB controller: To suppress the main longitudinal mode and improve ride comfort, a state FB controller is designed by the pole placement method to the following plant state-space model.

$$\dot{x} = A_c x + b_c F_{d,x}, \quad a_b = c_c x, \tag{14}$$

$$A_c = \begin{bmatrix} 0 & 1 \\ -\frac{M_u + M_b}{M_u M_b}K_{s,x} & -\frac{M_u + M_b}{M_u M_b}C_{s,x} \end{bmatrix},$$

$$b_c = \begin{bmatrix} 0 & \frac{1}{M_u M_b} \end{bmatrix}^{\mathrm{T}}, \quad c_c = \begin{bmatrix} K_{s,x} & C_{s,x} \end{bmatrix},$$

Since the state feedback controller requires the state variables, the state observer is designed in the discrete-time system as follows.

$$\hat{x}[i] = A_d\hat{x}[i-1] + b_d u[i-1] + K(y[i-1] - c_d\hat{x}[i-1]), \tag{15}$$

$$e[i] = x[i] - \hat{x}[i] = (A_d - Kc_d)e[i-1], \tag{16}$$

where A_d, b_d and c_d are obtained with zero-order holds of A_c, b_c, and c_c at sampling period T_s, u is input, y is output, $\hat{x}$ is estimated state variable vector, e is estimation error, and K represents the observer gain. Also, $x[i]$ indicates the x at the time iT_s.

Since the higher frequency range is dealt with in the proposed method, a dead time effect should be considered for further enhancement of control bandwidth. The dominant delay in automotive control systems is due to CAN communication. To avoid a reduction of phase margin by CAN, a state observer compensating dead time proposed in [25] is applied.

The dead time compensated observer can recover the phase margin by correcting the timing of the observer's estimation error term. The dead time compensated observer is formulated as follows.

$$\hat{x}[i] = A_d{}^n\hat{x}[i-n] + \begin{bmatrix} A_d{}^{n-1}b_d, \cdots, b_d \end{bmatrix} \begin{bmatrix} u[i-n] \\ \vdots \\ u[i-1] \end{bmatrix}$$
$$+ A_d{}^{n-1}K'(y[i] - c_{dead}\hat{x}[i-n] - d_{dead}u[i-n]), \tag{17}$$

$$e[i] = (A_d{}^n - A_d{}^{n-1}K'c_{dead})e[i-n], \tag{18}$$

$$c_{dead} = c_c e^{A_c(nT_s - T_d)}, \quad d_{dead} = \int_0^{nT_s - T_d} c_c e^{A_c\tau}b_c d\tau,$$

where T_d is the sum of input delay T_{di} and output delay T_{do}. Please note that the constant n is determined to satisfy $(n-1)T_s < T_d < nT_s$. In the experimental vehicle, the sampling time T_s is 4.096 ms and the identified dead time T_d is 11.4 ms as shown in Fig. 5d. Therefore, n is designed to be 3. By designing the observer gain K' such that the eigenvalues of $(A_d{}^n - A_d{}^{n-1}K'c_{dead})$ are in the unit circle, state variables are precisely estimated with less delay.

The state observer in the proposed method requires the sprung acceleration feedback, while the conventional method requires the relative velocity feedback. In the reference [15], the relative velocity is calculated by the integral of the relative acceleration obtained by the sprung and unsprung accelerometers. Since the mounting sensors on unsprung mass is not preferable due to complex cabling, the proposed method is

more practical from the view point of the required number and the place of accelerometers.
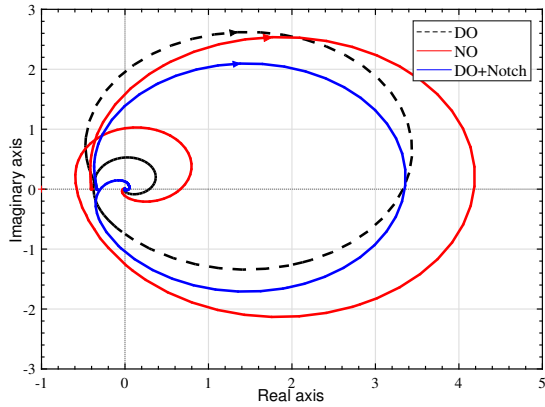

Fig. 7: Comparison of a Nyquist plot between the plant with the normal state observer (NO), that with the dead time compensated state observer (DO), and that with the dead time compensated state observer and notch filter (DO+Notch).
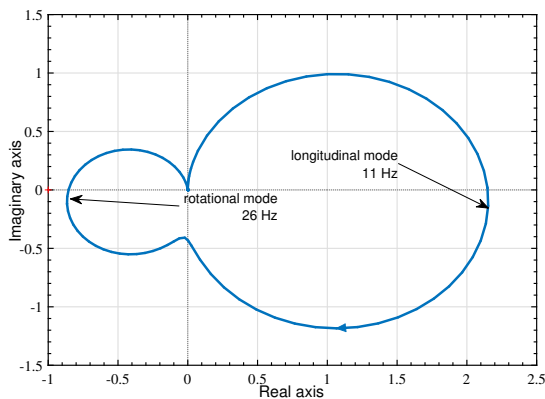

Fig. 8: Nyquist plot of the transfer function from driving force to relative velocity for open-loop characteristic analysis of conventional method.

V. SIMULATION ANALYSES

In simulations, the model identified in Fig. 5d is applied as a simulation plant to evaluate the control performance in longitudinal direction. Therefore, the both longitudinal and rotational modes effects are analyzed in simulations.

Firstly, the performance of the dead time compensated observer is evaluated in Fig. 7. The total delay is experimentally identified as 11.4 ms, while the sampling time is 4.096 ms. The dead time compensated state observer (DO) indicated by the black dotted line shows that the phase is recovered compared to the normal state observer (NO) indicated by the red solid line. The blue solid line shows the characteristics of the dead time compensated state observer with notch filter (DO+Notch). Gain stabilization is achieved by adding notch filter to the rotational mode.

Secondary, the Nyquist plot of the conventional method is indicated in Fig. 8. It shows that the stable margin of

the conventional method decreases as the feedback gain c_h increases. The stable margin is reduced by the rotational mode, which cannot be considered in the conventional method. Since the conventional method does not have enough number of controller parameters, the rotational mode cannot be suppressed. The conventional method cannot attenuate the longitudinal mode sufficiently, because the gain cannot increase due to the rotational mode.

Thirdly, Fig. 9a shows the comparison of the step responses of the body longitudinal acceleration between the conventional method and the proposed method. A step command with a value of 0.50 m/s^2 is input at 0.10 s as the black dotted line indicates. For Q_{FF} in the proposed method, five first-order low-pass filters with a cutoff frequency of 50 Hz are applied. These low-pass filters are experimentally designed to lower gain in high frequency range. The proposed method in magenta solid line shows a fast response without vibration, while the conventional method in the red dashed line shows large vibration. This is because the longitudinal mode is not sufficiently damped due to the lack of consideration of the rotational mode in the conventional method. Also, the robustness performance of the proposed method is evaluated in Fig. 9. The plant parameters used in the proposed method indicated in (15) are unsprung mass (M_u), sprung mass(M_b), suspension stiffness ($K_{s,x}$), suspension damping ($C_{s,x}$). The most variable parameter is the sprung mass, which is directly influenced by the weight of the passengers and the cargo. The simulations are conducted in two severe conditions; the evaluated sprung mass is nominal sprung mass (2000) ±500 kg. Since the simulations are conducted in the quarter-car model, the given sprung mass error is ±50 kg. The magnified view of the step responses with parameter error is shown in Fig. 9b. Although the performance is deteriorated by the modeling error, the proposed method shows the smoother responses than the conventional method, even with large modeling error.

Fourthly, frequency responses of the target response characteristic are shown in Fig. 10a. The conventional method in red solid line suppresses the longitudinal mode, but excites rotational mode. On the other hand, the proposed method in blue solid line shows high control bandwidth without the peaks.

VI. EXPERIMENTAL VALIDATION

The experiments are conducted with the vehicle in two conditions: shaking conditions and driving conditions.

A. Shaking conditions

In shaking conditions, an experiment is conducted on an even road surface to evaluate the motion performance. The experiment is step responses of the longitudinal acceleration starting from standstill.

Experimentally measured frequency responses of the target response characteristic are shown in Fig. 10b. The black dotted line indicates the frequency response without control. The conventional method in red solid line suppresses the longitudinal mode, but excites rotational mode. As in the simulation results

(a) Step responses.

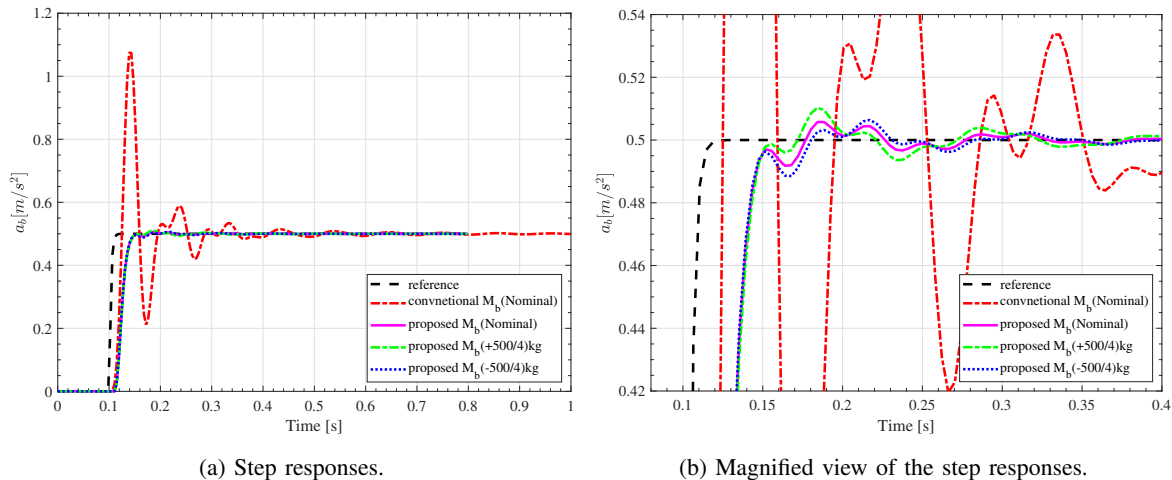

(b) Magnified view of the step responses.

Fig. 9: Simulation comparison of the longitudinal body acceleration in shaking condition by step responses.

shown in Fig. 10a, the proposed method in blue solid line shows high control bandwidth without the peaks.

Figure 11a shows the comparison of the PSD of the sprung accelerometer signal. The proposed method suppresses both modes, while the conventional method excites the rotational mode. Also, the suppression performance for the longitudinal mode in the conventional method is limited.

B. Driving conditions

In driving conditions, an experiment running over a road with disturbance is conducted to evaluate the ride comfort. The road is a test road for evaluation of ride comfort especially in relatively high frequency range. The experimental vehicle is ridden with four people. The proposed method and the conventional method are compared in the same time period on the same test road section. The vehicle velocity is controlled at 50 km/h with PI controller.

Figure 11b shows the PSD of the sprung longitudinal acceleration in driving condition. Both of the peaks at 11 Hz and 16 Hz appear, because both the motor torque and the road disturbances are input to the vehicle in this experimental condition. The conventional method suppresses the vibration at 11 Hz and 16 Hz, but excites the 26 Hz. The proposed method sufficiently suppresses all the modes, thus improving ride comfort.

Figure 12 shows the comparison of the PSD in different damping designs in the conventional method and the proposed method. The transfer function (13) shows that higher gain c_h leads to higher damping in the conventional method. The higher gain reduces stability margin of the system exciting the rotational mode at 26 Hz as seen in Fig. 12a. In Fig. 12b, the poles of the state feedback controller in the proposed method are changed such that only the damping term is changed. With higher damping design, the peaks at 11 Hz and 26 Hz are reduced while not exciting 26 Hz mode.

VII. CONCLUSION

Experimental identification of the frequency characteristics of the IWM vehicle is conducted in several conditions including a quarter-car motor bench, a four-poster test rig, and a test

vehicle driven on rough roads. The coupled dynamics model between rotational and longitudinal directions is proposed and validated through the frequency characteristics measurements. The model indicates that the increase in unsprung mass by IWM brings the longitudinal mode into the mid-frequency range (10 Hz), which cause discomfort and prevents from enhancing control bandwidth.

For a high motion performance and ride comfort, a longitudinal vibration suppression control method with high control bandwidth is proposed based on an obtained precise model. The proposed method includes a dead time compensated observer to recover the phase margin reduced by CAN communication. In experiments, the proposed method shows the fast acceleration responses while suppressing the longitudinal mode at 11 Hz and the coupled rotational mode around 26 Hz.

In this study, the driving force is approximated by the motor torque divided by the tire radius, though the wheel slip phenomena should be considered. Also, the coupled model between rotational and longitudinal directions has slip-ratio dependency. Therefore, driving force control should be applied to consider wheel slip effects in the future study. Moreover, in this study, only the coupled dynamics between rotational and longitudinal directions are considered. Our future studies will include the coupled dynamics with other degrees of freedom.

REFERENCES

[1] A. Martyn and H. Damian, "Unsprung mass with in-wheel motors-myths and realities," in *Int. Symposium on Advanced Vehicle Control (AVEC)*, pp. 261–266, Aug. 2010.

[2] V. Roel, B. Igo, and H. Nijmeijer, "Influence of in-wheel motors on the ride comfort of electric vehicles," in *Int. Symposium on Advanced Vehicle Control (AVEC)*, pp. 835–840, Aug. 2010.

[3] E. Tseng and D. Hrovat, "State of the art survey: Active and semi-active suspension control," *Vehicle System Dynamics*, vol. 53, pp. 1034–1062, May 2015.

[4] N. Amann, J. Bocker, and F. Prenner, "Active damping of drive train oscillations for an electrically driven vehicle," *IEEE/ASME Transactions on Mechatronics*, vol. 9, pp. 697–700, Dec. 2004.

[5] V. Ivanov, D. Savitski, J. Orus, J. M. R. Fortun, A. Sorniotti, and P. Gruber, "All-wheel-drive electric vehicle with on-board motors: Experimental validation of the motion control systems," in *IECON 2015*
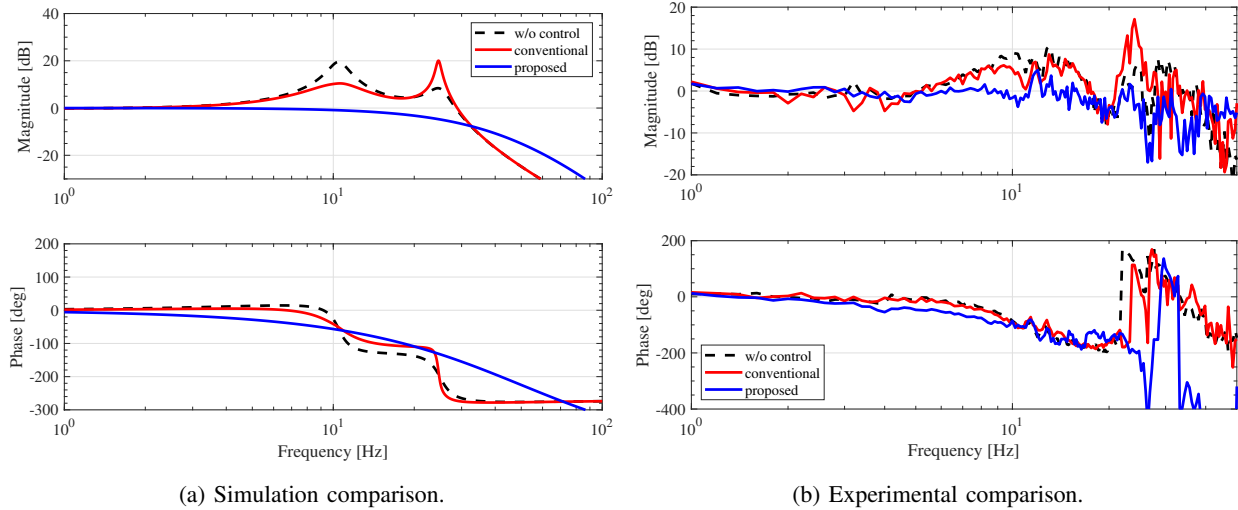
(a) Simulation comparison.

(b) Experimental comparison.

Fig. 10: Frequency characteristics of the longitudinal body acceleration (a_b/a_b^*) in shaking condition.

(a) PSD of the step responses in shaking condition.

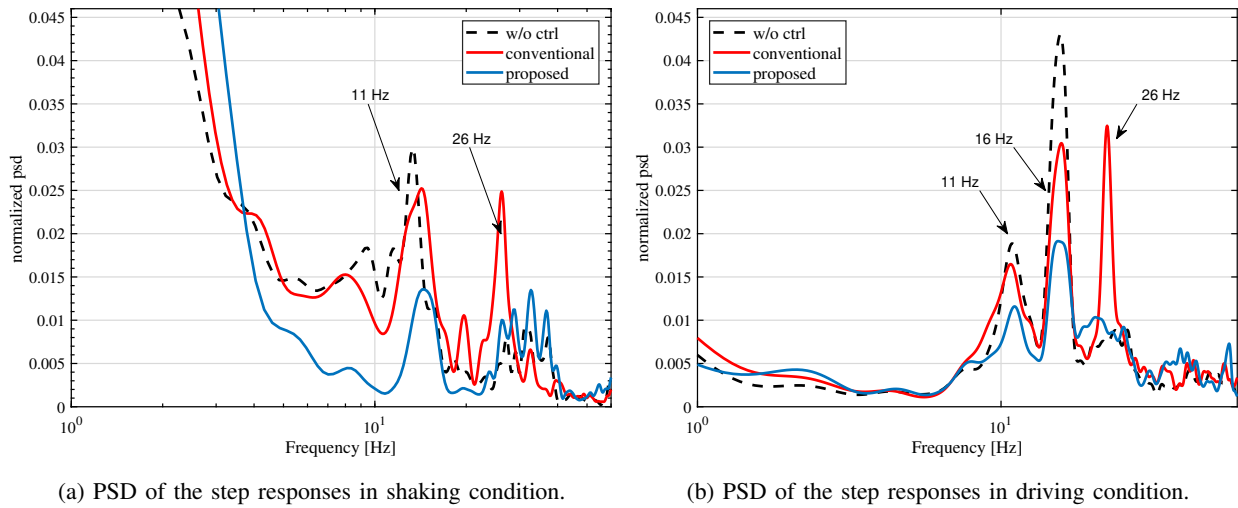(b) PSD of the step responses in driving condition.

Fig. 11: Experimental comparison of the longitudinal body acceleration (a_b) by step responses.

- *41st Annual Conference of the IEEE Industrial Electronics Society*, pp. 001729–001734, Nov. 2015.

[6] J. M. Rodríguez, R. Meneses, and J. Orús, "Active vibration control for electric vehicle compliant drivetrains," in *IECON 2013 - 39th Annual Conference of the IEEE Industrial Electronics Society*, pp. 2590–2595, Nov. 2013.

[7] S. Murata, "Innovation by in-wheel-motor drive unit," *Vehicle System Dynamics*, vol. 50, no. 6, pp. 807–830, 2012.

[8] N. Ochi, H. Fujimoto, and Y. Hori, "Proposal of roll angle control method using positive and negative anti-dive force for electric vehicle with four in-wheel motors," in *IEEE International Conference on Mechatronics (ICM)*, pp. 816–821, Feb. 2013.

[9] E. Katsuyama, "Decoupled 3D moment control for vehicle motion using In-Wheel motors," *SAE International Journal of Passenger Cars - Mechanical Systems*, vol. 6, pp. 137–146, Apr. 2013.

[10] M. Liu, F. Gu, and Y. Zhang, "Ride comfort optimization of in-wheel-motor electric vehicles with in-wheel vibration absorbers," *Energies*, vol. 10, no. 1647, pp. 1–21, 2017.

[11] X. Shao, F. Naghdy, and H. Du, "Reliable fuzzy hinf control for active suspension of in-wheel motor driven electric vehicles with dynamic damping," *Mechanical Systems and Signal Processing*, vol. 87, pp. 365–383, Nov. 2017.

[12] E. Katsuyama and A. Omae, "Improvement of ride comfort by unsprung negative skyhook damper control using In-Wheel motors," *SAE International Journal of Alternative Powertrains*, vol. 5, Apr. 2016.

[13] S. Ohno and K. Ito, "Unsprung vibration control for in-wheel-motor EV," in *JSAE Annual Congress (Autumn)*, no. 103, pp. 21–24, 2014.

[14] A. Takesaki, M. Kawafuku, M. Iwasaki, and T. Fujii, "Vibration suppression control system for electric vehicle considering longitudinal vibration," in *Proc. of IEEJ Technical Meeting Record*, no. 97, pp. 7–12, Mar. 2010.

[15] H. Fukudome, "Reduction of longitudinal vehicle vibration using In-Wheel motors," in *SAE Technical Paper Series*, Apr. 2016.

[16] D. Tan, Q. Wang, and Y. Wu, "Modal Analysis of In-Wheel Motor-Driven Electric Vehicle Based on Bond Graph Theory," *Shock and Vibration*, no. 6459154, 2017.

[17] A. J. Tuononen and A. Lajunen, "Modal analysis of different drivetrain configurations in electric vehicles," *Journal of Vibration and Control*, Mar. 2016.

[18] J. H. Montonen, N. Nevaranta, T. Lindh, J. Alho, P. Immonen, and O. Pyrhonen, "Experimental identification and parameter estimation of the mechanical driveline of a hybrid bus," *IEEE Transactions on Industrial Electronics*, vol. 65, pp. 5921–5930, Jul. 2018.

[19] T. Beauduin, S. Yamada, H. Fujimoto, T. Kanou, and E. Katsuyama, "Control-oriented modelling and experimental modal analysis of electric vehicles with geared In-Wheel motors," in *IEEE Int. Conf. Advanced Intelligent Mechatronics (AIM)*, pp. 541–546, Jul. 2017.

[20] S. Yamada, T. Beauduin, H. Fujimoto, T. Kanou, and E. Katsuyama, "Model-based longitudinal vibration suppression control for electric vehicles with geared in-wheel motors," in *IEEE Int. Conf. Advanced Intelligent Mechatronics (AIM)*, pp. 517–522, Jul. 2017.
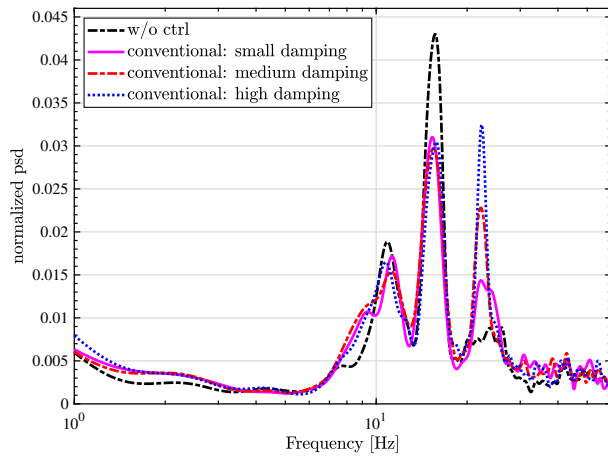
(a) Comparison in conventional method.
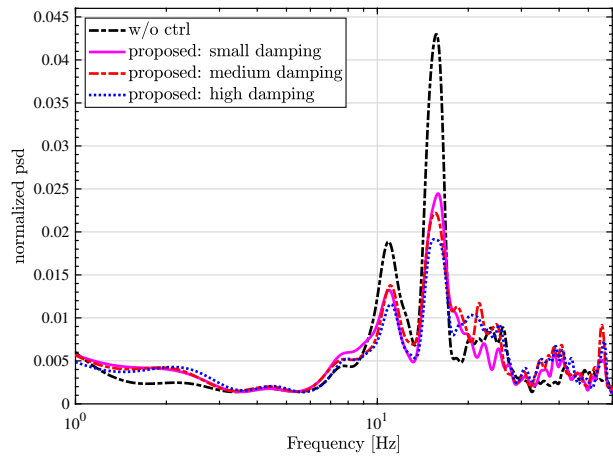
(b) Comparison in proposed method.

Fig. 12: Experimental comparison with different design designs in driving conditions.

[21] Y. Hori, "Future vehicle driven by electricity and control-research on four-wheel-motored "UOT electric march II"," *IEEE Transactions on Industrial Electronics*, vol. 51, pp. 954–962, Oct. 2004.

[22] K. Horinouchi, T. Yonekawa, T. Kanou, S. Utsumi, and Y. Nagahara, "Handling analysis with vehicle dynamics simulator," in *SAE Technical Paper Series*, Feb. 1997.

[23] ISO 8608:2016 "Mechanical vibration — Road surface profiles: Reporting of measured data".

[24] L. Soria, B. Peeters, and H. Van der Auweraer, "Operational modal analysis and the performance assessment of vehicle suspension systems," *Shock and Vibration Digest*, vol. 19, no. 5, pp. 1099–1113, 2012.

[25] H. Fujimoto and Y. Hori, "Visual servoing based on multirate control and dead-time compensation," *Advanced robotics: the international journal of the Robotics Society of Japan*, vol. 22, no. 6, pp. 780–787, 2004.

Hiroshi Fujimoto Hiroshi Fujimoto received the Ph.D. degree in the Department of Electrical Engineering from The University of Tokyo in 2001. In 2001, he joined the Department of Electrical Engineering, Nagaoka University of Technology, Niigata, Japan, as a research associate. From 2002 to 2003, he was a visiting scholar in the School of Mechanical Engineering, Purdue University, U.S.A. In 2004, he joined the Department of Electrical and Computer Engineering at Yokohama National University as a lecturer and became an associate professor in 2005. He joined the Department of Electrical Engineering at The University of Tokyo in 2010 as a Associate Professor, and became a Professor in 2021. He received the Best Paper Awards from the IEEE Transactions on Industrial Electronics in 2001 and 2013, Isao Takahashi Power Electronics Award in 2010, Best Author Prize of SICE in 2010, the Nagamori Grand Award in 2016, and First Prize Paper Award IEEE Transactions on Power Electronics in 2016. He was an associate editor of IEEE/ASME Transactions on Mechatronics from 2010 to 2014, IEEE Industrial Electronics Magazine from 2006, and IEEJ Transactions on Industrial Application from 2013, and Transactions on SICE from 2013 to 2016.

Shota Yamada Shota Yamada received the B.S. and M.S. degree in the Department of Electrical Engineering from The University of Tokyo in 2014 and 2016. He obtained his Ph.D. degree in the Department of Electrical Engineering and Information Systems at The University of Tokyo in 2019. In 2019, he joined NSK Ltd., Fujisawa, Japan. He is currently a project assistant professor of the Department of Advanced Energy in Frontier Sciences at The University of Tokyo since 2021.

Takeshi Kanou Takeshi Kanou received the B.S. and M.S. degrees in Yokohama National University, Yokohama, Japan in 2005 and 2007, respectively. He joins Toyota Motor Corporation, Aichi, Japan. He is engaged in the development of chassis control for mass production vehicles.

Thomas Beauduin received the B.S. and M.S. degree in Mechanical Engineering from the University of Leuven in 2012 and 2014, respectively. In 2014, he joined Hori-Fujimoto laboratory as a research assistant in the Department of Electrical Engineering and Information Systems at The University of Tokyo, Japan. Since 2017, he has been working as a senior research engineer for MTT in Canada.

Etsuo Katsuyama Etsuo Katsuyama received the B.S. degree in Tokyo Institute of Technology in 1997 and the Ph. D. degree in Kanagawa Institute of Technology in 2022. From 2007 to 2010, he joined Toyota Motorsport GmbH in Germany as a chassis engineer of formula 1. He currently works for Toyota Motor Corporation in Japan as a chassis engineer of passenger vehicles. He received the Arch T. Colwell Merit Award from the Society of Automotive Engineers in 2015, and the Outstanding Technical Paper Awards from the Society of Automotive Engineers of Japan in 2013, 2018, 2021 and 2022.